Nanoparticles for Photoacoustic Imaging of Vasculature

Min Zhou*, Lei Li*, Junjie Yao, Richard R. Bouchard, Lihong.V. Wang, and Chun Li

1 Introduction

Photoacoustic imaging (PAI), also referred to as optoacoustic tomography, is based on the measurement of ultrasonic waves induced by biological tissues that absorb short laser pulses. In PAI, light absorption by macromolecules, nanoparticles (NPs),

*Author contributed equally with all other contributors.

M. Zhou
Department of Cancer Systems Imaging, The University of Texas M. D. Anderson Cancer Center, 1881 East Road, Houston, TX 77054, USA

Institute of Translational Medicine, Zhejiang University, Hangzhou, Zhejiang 310009, China

L. Li
Department of Electrical and Systems Engineering, Washington University in St. Louis, One Brookings Dr., St. Louis, MO 63130, USA

J. Yao
Department of Biomedical Engineering, Washington University in St. Louis, One Brookings Dr., St. Louis, MO 63130, USA

R.R. Bouchard
Department of Imaging Physics, The University of Texas M.D. Anderson Cancer Center, Houston, TX, USA

L.V. Wang (✉)
Department of Electrical and Systems Engineering, Washington University in St. Louis, One Brookings Dr., St. Louis, MO 63130, USA

Department of Biomedical Engineering, Washington University in St. Louis, One Brookings Dr., St. Louis, MO 63130, USA
e-mail: lhwang@wustl.edu

C. Li (✉)
Department of Cancer Systems Imaging, The University of Texas M. D. Anderson Cancer Center, 1881 East Road, Houston, TX 77054, USA
e-mail: cli@mdanderson.org

J.W.M. Bulte, M.M.J. Modo (eds.), *Design and Applications of Nanoparticles in Biomedical Imaging*, DOI 10.1007/978-3-319-42169-8_16

or cells in the volume of interests creates a thermally induced pressure change that is translated to ultrasonic waves, which are received by acoustic detectors to form images. The technique combines the molecular specificity of optical imaging with the depth and spatiotemporal resolution of sonography. Unlike other high-resolution optical imaging modalities, PAI relies on orders of magnitude less scattered acoustic waves, which are induced by both diffused and ballistic light, and thus can be used to image deeper biological tissues. Photoacoustic effects were demonstrated in turbid medium by Kruger in 1994 [1], in biological tissues by Oraevsky et al. in 1997 [2], and in an in vivo small animal model by Wang et al. in 2003 [3]. Since then, PAI has been widely researched and advanced toward clinical applications [4].

Because of the overwhelming light-scattering effect of biological tissues, the photoacoustic signl-to-noise ratio (SNR) decreases exponentially with depth with a decay constant that is related to effective penetration depth. Light intensity attenuation can be minimized by choosing an excitation laser wavelength within the near-infrared (NIR) region, in which biological tissues have a relatively low absorption coefficient and a low scattering coefficient. Chromophores that absorb optical energy and convert it into acoustic signal are detected by PAI. A high optical absorption in NIR region increases detection sensitivity and thus extends imaging depth. The most important chromophores in the human body are oxyhemoglobin and deoxyhemoglobin. Hemoglobin has an absorption coefficient of over 100 cm^{-1} for visible light other than red; hence, it is capable of generating strong photoacoustic signals (~10 bars). Taking advantage of this endogenous contrast agent, PAI has been successfully applied to image vascular structures and tumor angiogenesis a few millimeters under the skin [5–7]. The technique has also been used to quantify oxygen hemoglobin saturation and thus the status of hypoxia in tumors [3, 8]. Ku et al. [7] demonstrated that hemoglobin in a blood sample 5 cm deep in biological tissues could be imaged. Attempts have also been made to apply PAI to the visualization of tumor vasculature in humans [9, 10].

Imaging tissue and tumor vasculature with a high penetration depth and high resolution is difficult to achieve without the use of appropriate exogenous contrast agents. In addition, optical contrast allows spectroscopic separation of signal contributions from multiple optical absorbers, thus enabling simultaneous functional imaging (with endogenous contrast from oxyhemoglobin and deoxyhemoglobin) and molecular imaging (with exogenous contrast agents). This concept was first demonstrated by in 2008 Li et al. [8]. In this study, PAI images of a tumor-associated biomarker and tumor oxygenation status based on exogenous and endogenous contrast agents were simultaneously acquired using multiple wavelengths around 800 nm in a mouse model. In recent years, various NPs have been studied as novel contrast agents for PAI. These NPs usually possess strong and tunable optical absorption in the NIR region. In this chapter, we provide an up-to-date summary of the PAI of tissue vasculature mediated by two classes of NPs, i.e., gold nanostructures and CuS NPs. We describe the structure, preparation, and in vivo application of these nanomaterials. We also touch upon the development of multimodal imaging, which includes PAI and other imaging modalities using multifunctional NPs for tumor vasculature imaging.

2 Principle of Photoacoustic Imaging

The photoacoustic effect is the generation of acoustic waves following light absorption in a medium. Generally, a short pulse of light is absorbed by chromophores in the medium and transiently converted to heat, which causes a rapid thermoelastic expansion that generates ultrasound waves [11]. Detection of the photon-induced ultrasonic wave yields a tomographic image. In order to efficiently generate ultrasound in biological tissue, normally a short-pulsed laser (typically, several nanoseconds pulse width) is used. The amplitude of the generated ultrasound signal is proportional to the original optical energy deposition with the conversion coefficient related to the thermal and mechanical properties of the tissue. Because the absorption of any photons regardless of their scattering histories can induce PA waves, PA signals can be generated in deep tissue. Ultrasonic scattering in tissue is three orders of magnitude weaker than optical scattering in the typical ultrasonic frequency range; high spatial resolution imaging can be achieved by the detection of PA waves. Consequently, PAI can break the optical diffusion limit.

The initial pressure induced by a sufficiently short laser pulse is given by

$$p_0 = \frac{\beta T}{\kappa}, \tag{1}$$

where β is the thermal coefficient of volume expansion, T is the temperature rise, and k is the isothermal compressibility. In soft tissue, a temperature rise of 1 mK induces approximately 800 Pa pressure rise, which is above the detection sensitivity of a typical ultrasonic transducer (~77 Pa for a 50 MHz transducer) [12]. Therefore, PAI is a highly sensitive imaging modality. If all absorbed light energy is converted to heat, the initial pressure can be expressed as

$$p_0 = \Gamma \mu_a F, \tag{2}$$

where Γ is the Grueneisen parameter, μ_a is the optical absorption coefficient (cm^{-1}), and F is the optical fluence (J/cm^2). PAI converts a fractional change in optical absorption to an identical fractional change in the PA signal, tantamount to a sensitivity of 100 % in the limit of small absorption variations. In principle, any molecule has its own absorption spectrum and thus can be imaged by PAI. Thus far, PAI has spectroscopically imaged many endogenous biological molecules, such as oxyhemoglobin, deoxyhemoglobin [13–15], melanin [16, 17], water [18–20], lipids [21–23], DNA and RNA [24, 25], and cytochrome [26, 27].

At depths beyond the optical diffusion limit, PAI can provide imaging with high ultrasound resolution, which is determined by the center frequency and bandwidth of the ultrasonic detection system and the bandwidth of the detected PA signal. The higher the central frequency and the broader the bandwidth, the better the spatial resolution. Penetration depths up to 5–6 cm have been reported using a safe laser exposure in the wavelength range of 600–1500 nm [28–30]. PAI scales spatial resolution with penetration depth, as shown in Fig. 1. With a detection central frequency of 50 MHz, acoustic-resolution photoacoustic microscopy has achieved a lateral resolution of 45 μm and an imaging depth of 3 mm [31]. Reducing the detection central frequency to 5 MHz expands the imaging depth to 4 cm and relaxes the resolution to 100–560 μm, depending on the detection geometry [32–35].

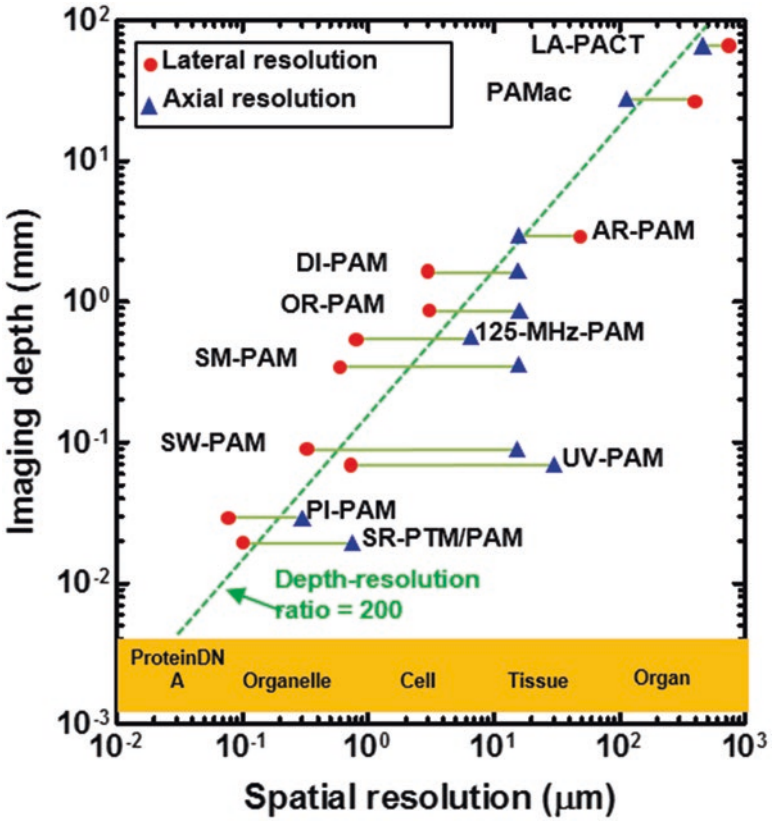

Fig. 1 Imaging depth versus spatial resolution in multi-scale PAI. The *red* circles represent lateral resolution, and the *blue* triangles denote axial resolution. LA-PACT, linear-array based PA computed tomography [80], PAMac, deep photoacoustic macroscopy [32]; AR-PAM, acoustic resolution photoacoustic microscopy (PAM) [81]; DI-PAM, double-illumination PAM [82]; OR-PAM, optical resolution PAM [14, 15, 83]; 125-MHz-PAM, PAM with a 125 MHz ultrasonic transducer [84]; SM-PAM, submicron PAM [85]; SW-PAM, subwavelength PAM [86]; UV-PAM, ultraviolet PAM [25]; PI-PAM, photo-imprint PAM [87]; SR-PTM/PAM, super-resolution photothermal/photoacoustic microscopy [88]

3 Why Nanoparticles

Without the introduction of exogenous contrast, PAI has been used in a variety of applications, including hemodynamic imaging [3, 36], blood oxygenation quantification [37], blood flow measurement [38], cancer detection [39], and tumor modeling [40, 41]. With appropriately chosen wavelengths, from the ultraviolet (UV) to visible (VIS) spectrum (250–700 nm), PAI can image cell nuclei, cytochromes, and red blood cells with high optical absorption contrast. However, UV and VIS light normally penetrates tissue only for hundreds of microns to millimeters, due to the

strong optical attenuation. In the NIR wavelength region (from 700 to 1100 nm), the optical absorption of tissue is at a minimum, which is called "optical window." The optical scattering in biological tissue decreases with increasing wavelength. Therefore, NIR light suffers the least optical attenuation, which gives PAI the greatest penetration. According to Eq. (2), the low endogenous optical absorption of NIR directly leads to weak PA signals, which affects the imaging sensitivity and depth. Therefore, the employment of exogenous contrast agents can greatly improve the imaging sensitivity, contrast, and specificity. Compared with endogenous molecules, exogenous contrast agents offer several advantages. First, the optical and chemical properties of exogenous contrast agents can be specifically engineered to maximize imaging contrast and detection sensitivity, and to minimize background absorption. Second, exogenous contrast agents can be specifically conjugated with targeting agents (e.g., peptides, antibodies, aptamers) to selectively bind to cell surface receptors. Third, exogenous contrast agents, especially NPs, can be engineered with specific structures for both PAI and localized therapy. For examples, the unique optical properties of these NPs can enable controlled drug delivery by light or ultrasound to the target organs and/or to mediate heat generation for thermal therapy.

A major concern for exogenous PA contrast agents is their photostability. Organic dyes suffer from permanent oxidative photobleaching and optically induced transient changes in their absorption spectrum. They are not suitable for quantitative PA measurement or applications which require high doses of laser energy or a long exposure time. In contrast, metal NPs, such as copper and nickel chloride, silica-coated plasmonic NPs [42, 43], and absorbing pigments, such as melanin from tyrosinase-expressing cells, have much better photostability.

4 Gold Nanostructures

Gold nanostructures, especially gold nanoshells, gold nanocages, gold nanorods, and hollow gold nanospheres, exhibit a unique and tunable optical property, termed surface plasmon resonance (SPR). SPR is a collective oscillation of conduction-band electrons within the structures induced by the oscillating dipole of a resonant wavelength of light. For solid spherical particles, the resonance peaks appear at approximately 520 nm for gold, and the peak varies slightly depending on the size of the particle and the embedding medium. The SPR peaks of nanostructures can be tuned from the VIS to the NIR region (650–1100 nm) by controlling the size, shape (e.g., nanorods), and structure (e.g., hollow or core–shell structured NPs). These unique optical properties combined with its excellent biocompatibility makes gold nanostructures well suited for PAI of vasculature [44].

Gold nanoshells (AuNS) consist of a dielectric or semiconducting core (i.e., silica) surrounded by an ultrathin gold shell. These nanostructures possess photothermal properties different from solid gold nanospheres of the same size. They have been shown to be useful for a variety of potential applications in photothermal ablation therapy and molecular optical imaging. Wang et al. [45] first reported brain

vasculature PAI imaging using AuNS with 100-nm silica cores, 20-nm gold shells, and with an 800-nm peak absorption. A deeply penetrating pulsed laser at 800 nm was employed to image the vasculature architecture of a rat brain. Compared to the brain PAI image based on the endogenous optical contrast, the image acquired ~20 min after three injections of the AuNS showed the brain vasculature with greater clarity. With the exogenous contrast agent, the optical absorption of the blood was increased and the contrast between the vessels and the background brain tissues was enhanced. By ~6 h after the third administration of AuNS, the optical absorption in the blood vessels decreased significantly. This was attributed to the clearance of the AuNS from the blood. The same group further reported high resolution reflection-mode (backward-mode) photoacoustic microscopy (PAM) that noninvasively imaged progressive extravasation and accumulation of AuNS within a solid tumor in vivo [46]. This study took advantage of the strong NIR absorption of AuNS that extravasated from leaky tumor vasculatures via the "enhanced permeability and retention" effect. With PAM, the three-dimensional AuNS distribution inside the tumor was visualized. Experimental results show that AuNS accumulated heterogeneously in tumors, with AuNS concentrated more in the periphery of the tumor and largely absent from the tumor core. This result is consistent with numerous other observations that drug delivery within tumor cores is ineffective because of poor blood perfusion.

Au nanocages are synthesized from Ag nanocubes by a galvanic replacement reaction [47, 48]. Similar to AuNS, the SPR absorption peak of Au nanocages can be tuned throughout the VIS and into the NIR region. Three sequential injections of Au nanocages in rats showed a gradual enhancement of the optical absorption in the cerebral cortex of brain by up to 81 % [47]. Compared with silica-cored AuNS, Au nanocages seem to have advantages for PAI due to their absorption-dominant extinction, more compact sizes (<50 nm), and larger optical absorption cross sections. Gold nanorods have also been employed as contrast enhancement agents for PAI owning to their strong absorption in the NIR range [49–55].

Hollow gold nanospheres (HAuNS) is a novel gold nanostructure consisting of only a thin Au wall with a hollow interior [56]. This type of gold nanostructures has the unique combination of being small in size (outer diameter, 40–50 nm), having spherical shape, a hollow interior, and a strong and tunable absorption band in the NIR region (Fig. 2). HAuNS are synthesized using cobalt (Co) instead of silver (Ag) NPs as sacrificial templates. The outer diameter of HAuNS is controlled by the diameter of the Co NPs, whereas the interior-cavity size is controlled by the stoichiometric ratio of $HAuCl_4$ and the reducing agents. HAuNS are coated with polyethylene glycol (PEG, MW 5000) to increase their blood circulation half-life. We evaluate the use of these PEGylated HAuNS as a contrast agent for PAI [57]. Our phantom study (Fig. 2d, e) revealed that the PAI of HAuNS was brighter than that of whole blood, aqueous solutions of $CuSO_4$ and India ink. Even though blood had optical density 2.3-fold greater than that of HAuNS in water suspension, the PA brightness of HAuNS was 2.5-fold greater than that of blood, indicating higher PA efficiency of HAuNS than that of blood.

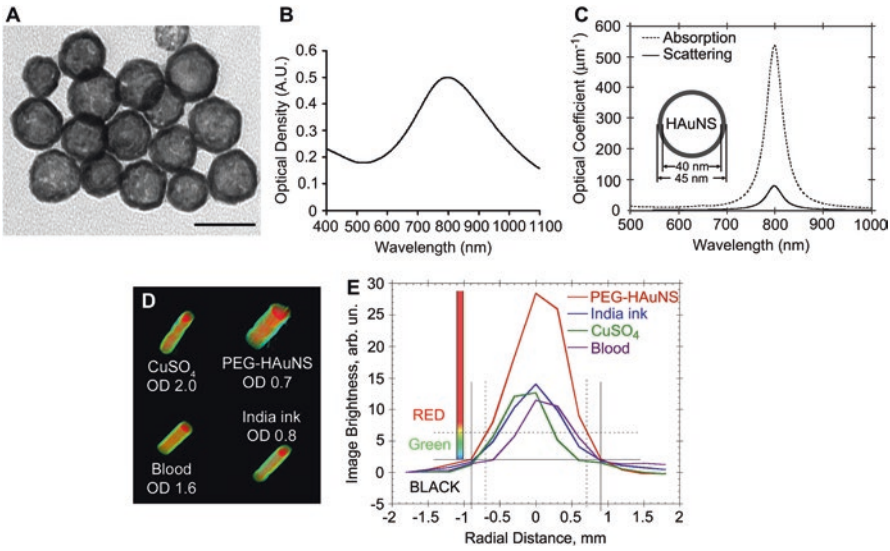

Fig. 2 (**a**) TEM image of PEG-HAuNS (Bar, 50 nm). The average outer diameter was 45 nm, and thickness of the shell was 2.5 nm. (**b**) Absorbance spectrum of PEGHAuNS in water, which peaked at 800 nm. (**c**) Theoretically calculated absorption and scattering spectra of PEG-HAuNS with water core having dielectric permittivity of 1.77. The inner core diameter was 40 nm and gold shell thickness was 2.5 nm, whose values are consistent with those shown in TEM. (**d**) Tomographic image of a tissue mimicking phantom made of poly(vinyl-chloride) plastisol with four embedded tubes filled with optically absorbing liquid media. (**e**) Quantitative analysis of the photoacoustic image brightness through the cross-section of each tube from (**d**). The color scale was designed in three steps: from *black* to *blue*/*green* to *red*. All tubes with different levels of brightness reflected in the object diameter. Reprinted with permission from Ref. [57]

PAI of the cerebral cortex of a mouse before contrast injection showed only large vessels (e.g., the middle cerebral artery, distributed along the mouse brain cortical surface) (Fig. 3a, arrow). This is because oxyhemoglobin and deoxyhemoglobin display weak PA signal at 800 nm. However, 5 min after the injection of PEGylated HAuNS, the PAI image revealed the brain vasculature with much greater clarity, especially for small blood vessels (Fig. 3b, c). This enhanced clarity was attributed to the strong PA signal generated with HAuNS. This is better appreciated in differential images (Fig. 3d, e) obtained by subtracting the preinjection image from the postinjection images pixel by pixel. At 2 h post-injection, the PA images remained essentially unchanged, indicating a significant amount of HAuNS circulating in the blood (Fig. 3c, e). At higher magnification, PAI revealed not only the structure of large vessels (Fig. 4a, yellow-framed picture) but also small blood vessels (Fig. 4a, green-framed pictures) 2 h after HAuNS injection. Indeed, brain blood vessels in the superficial cortex as small as ~100 μm in diameter could be clearly seen (Fig. 4a, arrows). HAuNS were confirmed to be located on the luminal

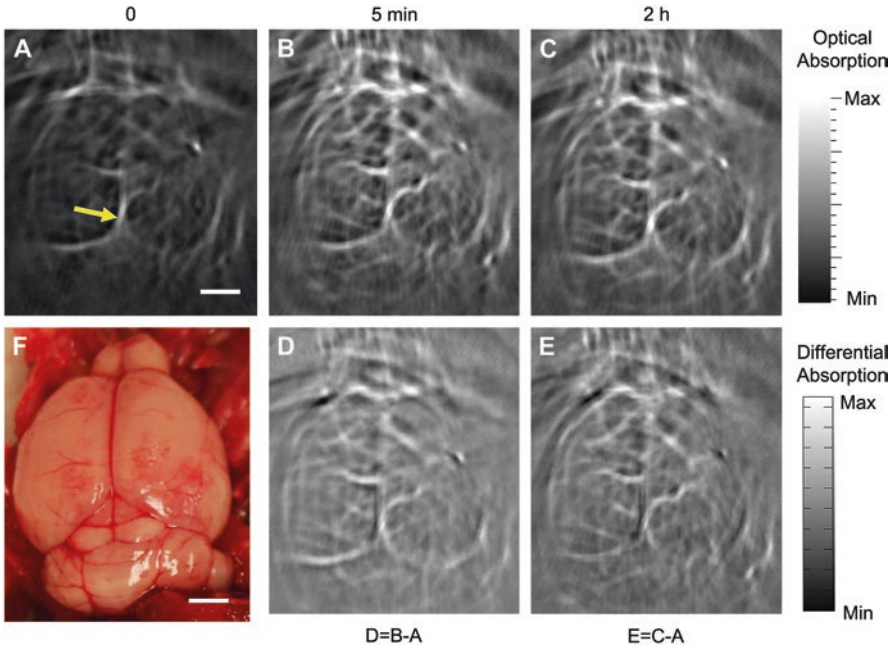

Fig. 3 Noninvasive PAI imaging of a mouse brain in vivo employing PEG-HAuNS and NIR light at a wavelength of 800 nm. Photoacoustic image acquired (**a**) before, (**b**) 5 min after, and (**c**) 2 h after the intravenous injection of PEG-HAuNS. (**d**, **e**) Differential images that were obtained by subtracting the preinjection image from the post-injection images (Image **d** = Image **b**–Image **a**; Image **e** = Image **c**–Image **a**). *Arrow*, middle cerebral artery. Bar = 2 mm. (**f**) Open-skull photograph of the mouse brain cortex obtained after the data acquisition for PAI. Bar = 2 mm. Reprinted with permission from Ref. [57]

side of the blood vessels (Fig. 4b, c). There was no particle extravasation into the brain parenchyma. This was attributed to the blood–brain barrier, which has been shown to impede the penetration of such particles. Thus, the long-circulating PEG-HAuNS enhanced the contrast between the blood vessels and the brain parenchyma [57].

Integrin αvβ3 is known to be overexpressed in the angiogenic blood vessels of solid tumors. Lu et al. [58] showed that intravenous injection of cyclic peptide c(KRGDf)-coated HAuNS targeting αvβ3 permitted PAI of orthotopically inoculated U87 glioma in nude mice (Fig. 5). Quantitative analysis confirmed that the mean PA signal ratio between the tumor and the contralateral normal brain at 24 h after c(KRGDf)-HAuNS injection was approximately twice as high as that obtained from precontrast images (without contrast agent injection). In comparison, no change in PA signal ratio between the tumor and the normal brain was observed before and after intravenous injection of the nonspecific PEG-HAuNS (Fig. 5). These data indicate that selective binding of c(KRGDf)-HAuNS to both tumor cells and tumor endothelial cells enhanced PAI of U87 glioma. c(KRGDf)-HAuNS also

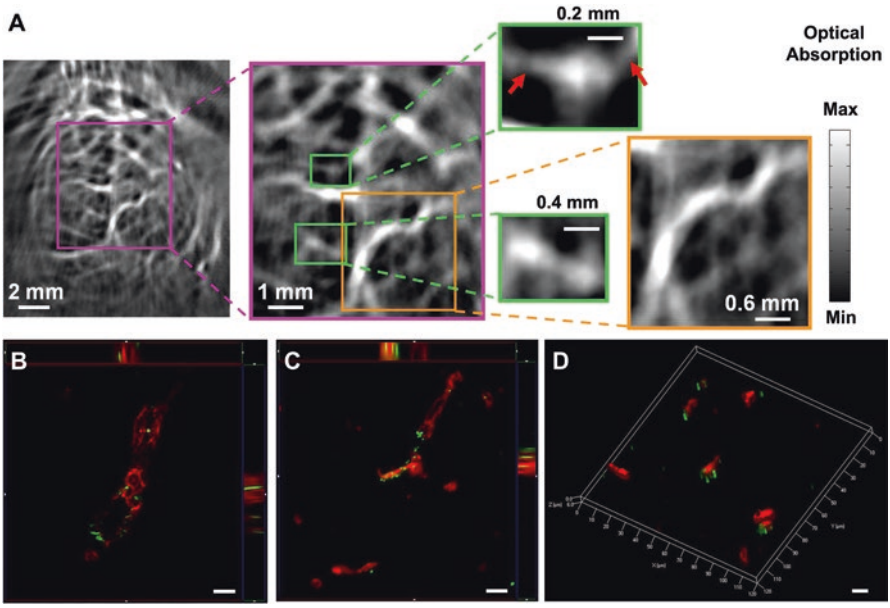

Fig. 4 (**a**) Enhanced PA signals revealed clear and detailed structure of large (*yellow*-framed picture) and small (*green*-framed picture) blood vessels in the mouse brain at higher magnification 2 h after intravenous injection of PEG-HAuNS. *Arrows* represent the small blood vessels with a diameter of about 100 μm, which can be seen in the contrast-enhanced images. (**b**–**d**) Distribution of PEG-HAuNS in brain vessels 2 h after injection (Bar = 10 μm). Brain vessels were stained with anti-CD31 antibody (*red* fluorescence), while the scattering signals of gold particles were detected under a dark field (pseudo-green). Z-stack images showed the particles located on the luminal side of brain blood vessels (**b**, **c**). In brain capillaries, three-dimensional reconstruction images show that the particles colocalized or stayed adjacent to the brain capillary endothelial cells (**d**). Reprinted with permission from Ref. [57]

mediated a selective photothermal ablation of U87 tumor, leading to a significant increase in overall survival of tumor-bearing mice compared to mice treated with laser alone or c(KRGDf)-HAuNS alone [58]. These results suggest that PAI may be used to guide photothermal ablation therapy mediated by the same nanoparticle targeted to tumor vasculature and tumor cells.

By integrating multiple functions into a NP's design, it is possible to use the same nanostructure for multimodality imaging applications. Along this line of research, Zhou et al. [59] reported dual PAI and magnetic resonance imaging (MRI) after intravenous administration of superparamagnetic iron oxide (SPIO)-containing gold nanoshells (SPIO@AuNS). Here, PAI was used to delineate tumor vasculature, while T2-weighted MRI was used to monitor therapeutic effects after photothermal therapy mediated by SPIO@AuNS. Gadolinium (Gd)-doped, gold-speckled silica NPs were synthesized as multimodal nanoparticulate contrast agents for noninvasive imaging using both PAI and T1-weighted MRI [60].

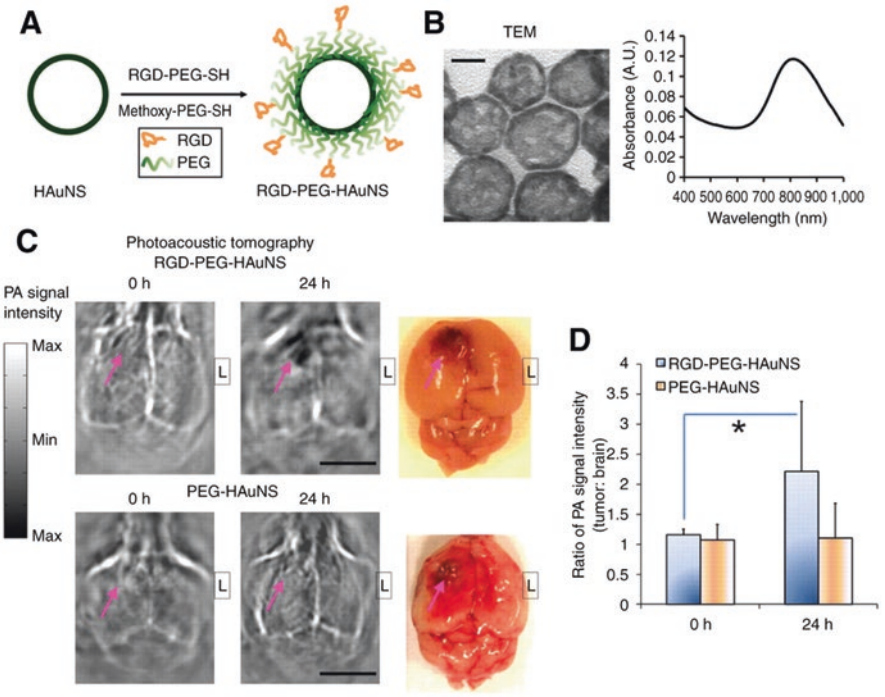

Fig. 5 (**a**) Scheme for c(KRGDf)-PEG-HAuNS bioconjugation. (**b**) c(KRGDf)-PEG-HAuNS characteristics on transmission electron microscopy (bar, 20 nm) and UV–Vis spectrum (measured in water). (**c**) PAI images of U87 human glioma in mouse brains before (0 h) and 24 hours after i.v. injection of NPs (bar, 5 mm). Photographs of corresponding mouse brains were used to confirm tumor location. *Arrows*, locations of tumors; *L* left. (**d**) PA signal intensity ratio of tumor-to-contralateral brain in mice before (0 h) and 24 h after injection of HAuNS. Data arepresented as mean = SD. c(KRGDf)-PEG-HAuNS group, $n = 5$; PEG-HAuNS group, $n = 4$. *, significant difference between precontrast and 24-h postcontrast groups ($p < 0.05$). Reprinted with permission from Ref. [58]

5 Copper Sulfide Nanoparticles and Carbon Nanotubes

NIR light at 1064 nm lies on the second window in the NIR region that encounters less tissue attenuation by the absorption of hemoglobin and water. Among the pulsed lasers emitting NIR light, the Q-switched Nd:YAG laser, which emits laser light at 1064 nm, can provide high pulsed energy with a nanosecond pulsed widths. In fact, its second harmonic radiation at 532 nm is usually employed to pump other lasing media, such as Ti:Sapphire, to obtain tunable laser output in the NIR region. The laser energy conversion efficiency is characteristically around 10 % (~50 % of second harmonic generation and ~20 % of other lasing media). This means that with a typical laser output of ~1 J/pulse at 1064 nm from a commercial Q-switched Nd:YAG laser, only ~100 mJ/pulse maximum output can be obtained at 800 nm, which is within the first biological tissue window. With 10 times greater available

laser pulse energy, a 1064-nm laser would have a much higher fluence rate than that of an 800-nm laser pulse (which is generated with a 532-nm pump and an additional lasing medium) at a depth ≤50 mm. Higher laser energy should translate to a stronger PA signal, higher SNR, and greater field-of-view. However, at 1064 nm, blood vasculature or tumor cells have little specific optical absorption that clearly distinguishes them from other normal organ structures.

Towards the goal of enhancing the sensitivity and specificity of PAI at the 1064 nm wavelength, we recently reported the use of copper sulfide NPs (CuS NPs) as a new class of contrast agent for deep-tissue PAI. CuS NPs display optical absorption tunable to 1064 nm and are much smaller (diameter <15 nm) than plasmonic Au nanostructures, which should be preferable for imaging extravascular tumor cells [61]. CuS NPs are readily synthesized in aqueous solution by reacting $CuCl_2$ and Na_2S in the presence of various stabilizers [62, 63]. Preliminary PAI studies were conducted with PEG-coated CuS NPs dispersed in 10 % polyacrylamide gel embedded in fresh chicken breast. The CuS NP targets in this phantom could be clearly visualized at ~5 cm depth from the laser irradiation surface. Figure 6 shows in vivo PAI images of a mouse brain acquired with green light at 532 nm without exogenous contrast (Fig. 6a) and with NIR light at 1064 nm using PEGylated CuS NPs as a contrast agent (Fig. 6b, c). Hemoglobin is the major chromophore in biological tissues and has strong absorption of green light at 532 nm. As has been shown before with PEG-HAuNS (Fig. 5), the superficial vascular structures of the mouse brain, such as the veins and arteries in the cerebral and temporal lobes, could be clearly visible with green light (Fig. 6a). However, green light cannot penetrate deeply because of strong tissue absorption and scattering at short wavelengths. On PAI images of the mouse brain acquired at 1064 nm, only the sagittal and transverse sinuses were visualized; blood vessels were not discernible because of the lack of contrast between blood vessels and the brain parenchyma (Fig. 6b, c). A nodule on the left cerebral cortex that was injected intracranially with 15 μL of an aqueous solution of CuS NPs (2 OD) 24 h before PAI acquisition was clearly seen, which dissolved 7 days after CuS NP injection because CuS NPs were cleared from the injection site (Fig. 6b, c). These studies confirm that CuS NPs were effective PAI contrast agent at 1064 nm and may be used for molecular PAI imaging of tumor and angiogenic blood vessels when these NPs are decorated with appropriate ligands.

The blood vessel network of a tumor regulates the supply of nutrients and oxygen to the cancer cells, affects their survival and growth, and influences the response of the tumor to therapy. Noninvasive in vivo studies of the tumor blood vasculature are therefore of interest in fundamental cancer research and the development of new drugs and other therapies. To test whether PEG-CuS NPs can be used as an exogenous contrast for PAI of tumor vasculature, we used the orthotopic 4 T1 mammary tumor model. Without contrast agent, several large vessels could be seen, probably due to light absorption by hemoglobin and water molecules at 1064 nm (Fig. 7a) [64]. However, smaller blood vessels are not discernible. At 5 min and 2 h after intravenous injection of PEG-CuS NPs (2 OD), blood vessel structures, including smaller vessels, were more clearly visualized (Fig. 7b, c), indicating increased vasculature contrast after PEG-CuS NP injection. PAI images acquired at 1064 nm

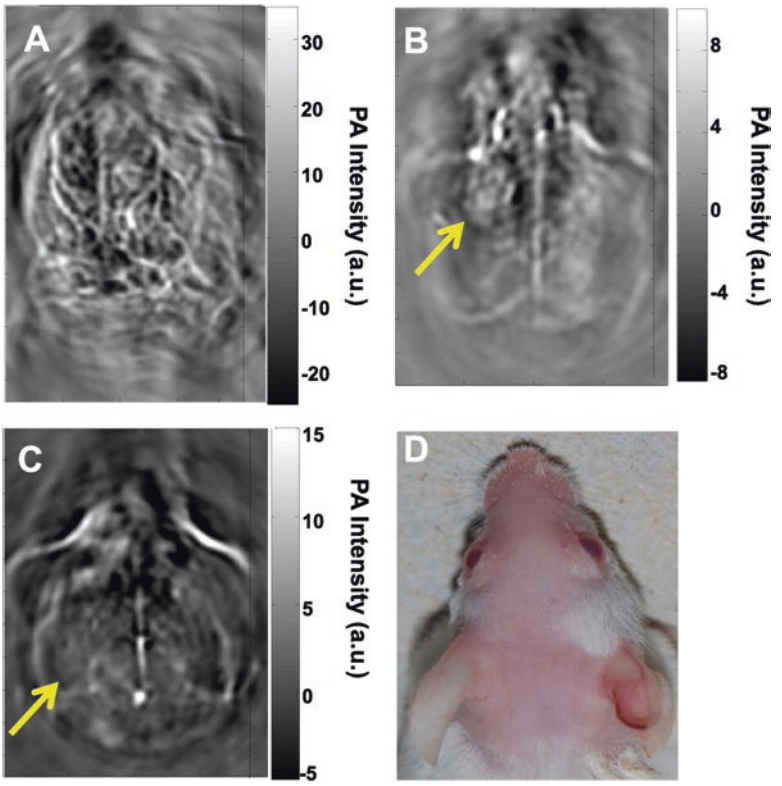

Fig. 6 Representative in vivo PAI images of a mouse brain. Images were acquired using laser light (**a**) at a wavelength of 532 nm without exogenous contrast, (**b**) at 1064 nm 24 h after intracranial injection of 15 µL of CuS NP solution, and (**c**) at 1064 nm 7 days after intracranial injection of 15 µL of CuS NP solution. (**d**) Photograph of the head of the mouse. Laser light was delivered from the top. Reprinted with permission from Ref. [61]

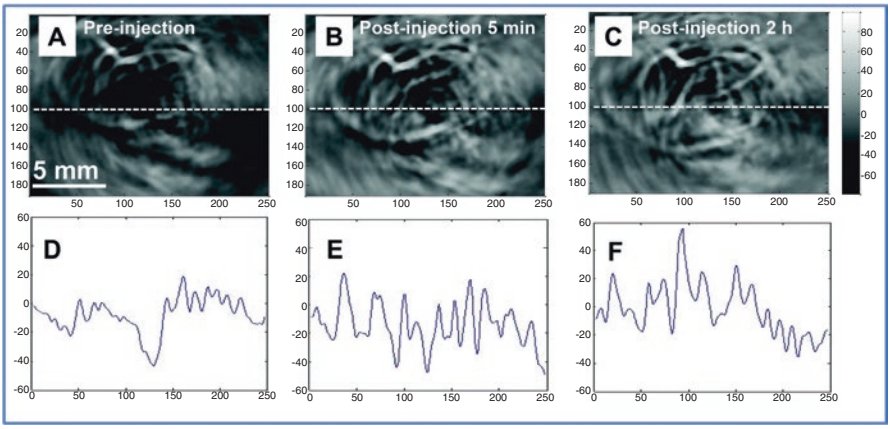

Fig. 7 Representative in vivo PAI images of a 4T1 mammary tumor grown in the mammary fatpad and corresponding PA signals ($n=3$). Images were acquired using ns-pulsed laser light at a wavelength of 1064 nm (**a**) before CuS NP injection, (**b**) 5 min after intravenous injection of 200 µL of CuS NP solution (100 µg mL−1, 2 OD), and (**c**) 2 h after intravenous injection of 200 µL of CuS NP solution. (**d**–**f**) PA signal traces correspond to the white lines in the respective PA images. Reprinted with permission from Ref. [64]

with PEG-CuS NPs suggest that this contrast agent is a promising platform for PAI of tumor blood vessels. An interesting aspect of the studies by Zhou et al. [64] was the incorporation of ^{64}Cu, a positron emitter to the same CuS NP matrix without the use of any radiometal chelator, which permitted simultaneous micro-positron emission tomography (μPET) imaging and quantification of tumor uptake of PEG-CuS NPs. Such a dual-modality imaging approach enabled by a single contrast agent is expected to provide much needed complimentary information that cannot be readily acquired with a single imaging modality.

Several other attempts have been made to increase signal intensity for PAI contrast agents. For example, conjugating small optical dye molecules to single-walled carbon nanotubes (SWNT-dye) led to sub-nanomolar sensitivity for PAI [65]. The dyes used for conjugation includes indocyanine green (ICG), methylene blue (MB), QSY_{21} (QSY), and cyanine (Cy5.5). Studies have shown that dye-containing SWNT had much higher optical absorption in the far red and NIR region than SWNT without dyes. Tumors in mice injected with RGD peptide-coated, dye-conjugated SWNT targeted integrin αvβ3 in angiogenic blood vessels, leading to a threefold increase in PA signal intensity compared to tumors in mice injected with the untargeted SWNT-dye [65]. These and other studies demonstrate that with appropriate nanoparticle design, it is possible to improve the sensitivity of PAI to picomolar concentration [51, 57, 66].

6 PA Imaging of Sentinel Lymph Nodes and Atherosclerotic Plaques

In addition to imaging vasculature and tumor blood vessels, various gold nanostructures are also studied as possible PAI contrast agents for mapping of sentinel lymph nodes (SLNs) [48, 55], ex vivo imaging of joint tissue [67], monitoring of drug release [68], and characterization of macrophages in atherosclerotic plaques [69, 70]. PAI of SLNs is worth noting in particular. The SLN, the first lymph node receiving drainage from the tumor is believed to be most likely to be positive for metastases. SLN biopsy has been used in the clinic as the preferred method for tumor staging. Before a biopsy can be taken for staging purposes, SLN must be identified. Current methods for SLN mapping typically use a blue dye (e.g., isosulfan blue or methylene blue) or radioactive colloids (e.g., technetium-99 or ^{99m}Tc). However, these approaches require either invasive techniques to visualize the blue stain or specialized facilities to deal with potentially hazardous radioactive components. Therefore, techniques such as PAI that can map SLNs without surgery or radioactivity are highly desirable. Using Au nanocages as the PAI contrast agent, Song et al. [48] have shown that SLNs could be readily imaged with PAI in the context of the surrounding vasculature and within ~3 mm below the skin surface of a rat (Fig. 8). By placing chicken breast tissue on top of the rat skin, a further study showed that the SLN could be imaged with good contrast as deep as 33 mm below the skin surface, which is significantly deeper than the ~12 mm depth of SLNs in humans.

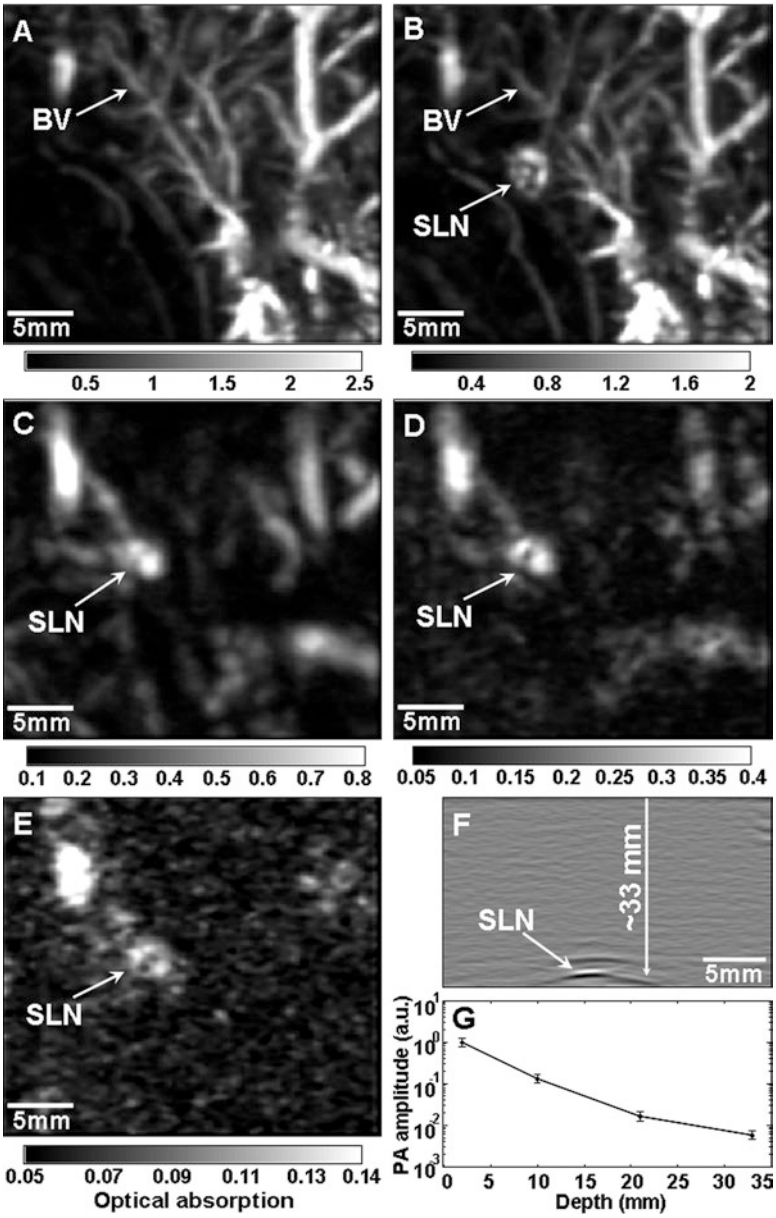

Fig. 8 Depth capability of noninvasive PA SLN mapping in another rat, demonstrating potential for clinical use. PA sagittal MAP images before (**a**) and after (**b–e**) the injection: (**a**) control image; (**b**) 28 min; (**c**) 126 min with a layer of chicken breast tissue placed on axillary region, providing a total imaging depth of 10 mm; (**d**) 165 min with the second layer of chicken breast tissue, providing a total imaging depth of 21 mm; (**e**) 226 min with the third layer of chicken breast tissue, providing a total imaging depth of 33 mm. (**f**) PA B-scan with 20 times signal average, showing the SLN located 33 mm deep. Memory of the acquisition system limited the record length in depth. (**g**) Amplitude variations of PA signals over imaging depths. Data were scaled down to 0 dB and normalized by the maximum. Error bar represents standard deviation. All images were acquired without signal averaging except the B-scan (**f**). Colorbars represent the optical absorption. *BV* blood vessel, *SLN* sentinel lymph node. Reprinted with permission from Ref. [48]

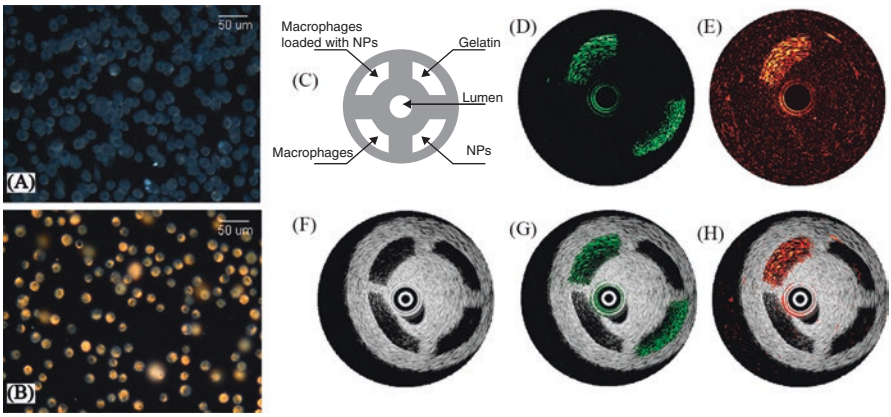

Fig. 9 Optical images of (**a**) intact murine macrophages and (**b**) murine macrophages conjugated with gold NPs. (**c**) Diagram of the tissue-mimicking phantom and (**f**) the corresponding intravascular ultrasound (IVUS) image. IVPA images of the same cross-section of the phantom taken at (**d**) 532 nm and (**e**) 680 nm. Overlaid IVUS and IVPA images of the phantom acquired at (**g**) 532 nm and (**h**) 680 nm, indicating the origin of the PA responses in the upper-left quadrants of the IVPA images. Reprinted with permission from Ref. [69]

Plasmonic gold NPs (Au-NPs) have been investigated as a contrast agent for macrophage detection in atherosclerotic plaques. The aggregation of Au-NPs internalized by macrophages causes a red shift in the particles' optical absorption spectrum. By utilizing enhanced absorption induced by plasmon resonance coupling, intravascular photoacoustic (IVPA) imaging at 680 nm can detect the signal from macrophages highlighted by aggregated Au-NPs (Fig. 9) [69, 71]. Here, the spectral difference in optical absorption between the aggregated and non-aggregated Au-NPs offers a mechanism to image macrophages. By employing multiwavelength measurements, IVPA imaging of a tissue phantom shows that aggregated NPs can be differentiated from the surrounding tissue. Thus, it is possible to identify the presence and the location of NPs associated with macrophage-rich atherosclerotic plaques.

7 Summary and Outlook

PAI imaging is a powerful and emerging noninvasive hybrid modality which provides three-dimension imaging with high spatial resolution. PAI with vasculature contrast agents can be used to perform noninvasive angiography, assess angiogenesis, quantify and measure the spacing of blood vessels, and measure blood volume and flow. PA signal amplitudes can be greatly enhanced with exogenous contrast agents, especially those leveraging NPs with strong absorption in the NIR region. These NPs usually display large absorption cross sections within the optical window of biological tissues. They have been successfully applied as intravascular contrast agents for PAI in various animal models to enhance the contrast between blood

and surrounding tissues, allowing more detailed vascular structures to be imaged at greater depths. Combined with NIR light absorbing NPs decorated with ligands directed at tumor cell surface receptors, these NPs provide not only a promising platform for vasculature imaging, but also the opportunity for molecular PAI imaging. However, there are still some challenges in translating these techniques into clinical use. For example, to be clinically relevant, the penetration depth of the PAI imaging, the high cost of nanomaterials' preparation, and the toxicity of the nanomaterials currently present unresolved concerns. Recent attempts to reduce potential long-term side effects of nanoparticle-based PAI contrast agents have been made with some success by developing renally clearable NPs. For example, we reported the synthesis and characterization of ultrasmall CuS NPs (diameter <6 nm) that can be readily cleared from the body via the renal-urinary route over a period of 24 hours [72]. Song et al. [73] reported Au nanorods (dimension: ≈8 nm × 2 nm) embedded in biodegradable poly(lactic-co-glycolic acid) NPs (~60 nm in diameter) that could be cleared from the body over a period of 10 days. These NPs may be adapted for PAI because they all have strong absorption in the NIR region. Through synergistic combination with other imaging modalities (i.e., Raman imaging, MRI, PET), PAI may offer complementary information with greater resolution and/or detection sensitivity [74–79]. Successful translation of PAI to the clinic requires a practical PAI system that efficiently penetrates biological tissues and a contrast agent with optical absorption peaks at or near the wavelength of the laser source. It is expected that progress on both of these fronts will eventually make it possible to introduce PAI to the clinic for guiding individualized therapy for cancer patients.

Acknowledgements This work is supported in part by the John S. Dunn Foundation (CL), by the US National Institutes of Health grants DP1 EB016986 (NIH Director's Pioneer Award, LHW), R01 CA186567 (NIH Director's Transformative Research Award, LHW), and U01 NS090579 (BRAIN Initiative, LHW). L.V. Wang has a financial interest in Endra, Inc., and Microphotoacoustics, Inc., which, however, did not support this work. The other authors declare no competing financial interests.

References

1. Kruger RA. Photoacoustic ultrasound. Med Phys. 1994;21:127–31.
2. Oraevsky AA, Jacques SL, Tittel FK. Measurement of tissue optical properties by time-resolved detection of laser-induced transient stress. Appl Opt. 1997;36:402–15.
3. Wang XD, Pang YJ, Ku G, Xie XY, Stoica G, Wang LHV. Noninvasive laser-induced photoacoustic tomography for structural and functional in vivo imaging of the brain. Nat Biotechnol. 2003;21:803–6.
4. Wang LHV, Hu S. Photoacoustic tomography: in vivo imaging from organelles to organs. Science. 2012;335:1458–62.
5. Jose J, Manohar S, Kolkman RGM, Steenbergen W, van Leeuwen TG. Imaging of tumor vasculature using Twente photoacoustic systems. J Biophotonics. 2009;2:701–17.
6. Kolkman RGM, Hondebrink E, Steenbergen W, de Mul FFM. In vivo photoacoustic imaging of blood vessels using an extreme-narrow aperture sensor. IEEE J Sel Top Quant. 2003;9:343–6.

7. Ku G, Wang XD, Xie XY, Stoica G, Wang LHV. Imaging of tumor angiogenesis in rat brains in vivo by photoacoustic tomography. Appl Opt. 2005;44:770–5.
8. Li ML, Oh JT, Xie XY, Ku G, Wang W, Li C, et al. Simultaneous molecular and hypoxia imaging of brain tumors in vivo using spectroscopic photoacoustic tomography. Proc IEEE. 2008;96:481–9.
9. Ermilov SA, Khamapirad T, Conjusteau A, Leonard MH, Lacewell R, Mehta K, et al. Laser optoacoustic imaging system for detection of breast cancer. J Biomed Opt. 2009;14:024007.
10. Manohar S, Vaartjes SE, van Hespen JCG, Klaase JM, van den Engh FM, Steenbergen W, et al. Initial results of in vivo non-invasive cancer imaging in the human breast using near-infrared photoacoustics. Opt Express. 2007;15:12277–85.
11. Wang LV. Photoacoustic tomography. Scholarpedia. 2014;9:10278.
12. Yao J, Wang LV. Sensitivity of photoacoustic microscopy. Photoacoustics. 2014;2:87–101.
13. Ray A, Rajian JR, Lee YE, Wang X, Kopelman R. Lifetime-based photoacoustic oxygen sensing in vivo. J Biomed Opt. 2012;17:057004.
14. Maslov K, Zhang HF, Hu S, Wang LV. Optical-resolution photoacoustic microscopy for in vivo imaging of single capillaries. Opt Lett. 2008;33:929–31.
15. Li L, Yeh CH, Hu S, Wang LD, Soetikno BT, Chen RM, et al. Fully motorized optical-resolution photoacoustic microscopy. Opt Lett. 2014;39:2117–20.
16. Forest SE, Simon JD. Wavelength-dependent photoacoustic calorimetry study of melanin. Photochem Photobiol. 1998;68:296–8.
17. Viator JA, Komadina J, Svaasand LO, Aguilar G, Choi B, Nelson JS. A comparative study of photoacoustic and reflectance methods for determination of epidermal melanin content. J Investig Dermatol. 2004;122:1432–9.
18. Szakall M, Huszar H, Bozoki Z, Szabo G. On the pressure dependent sensitivity of a photoacoustic water vapor detector using active laser modulation control. Infrared Phys Technol. 2006;48:192–201.
19. Xu Z, Li C, Wang LV. Photoacoustic tomography of water in phantoms and tissue. J Biomed Opt. 2010;15:036019.
20. Xu Z, Zhu Q, Wang LV. In vivo photoacoustic tomography of mouse cerebral edema induced by cold injury. J Biomed Opt. 2011;16:066020.
21. Allen TJ, Hall A, Dhillon AP, Owen JS, Beard PC. Spectroscopic photoacoustic imaging of lipid-rich plaques in the human aorta in the 740 to 1400 nm wavelength range. J Biomed Opt. 2012;17:061209.
22. Wang B, Karpiouk A, Yeager D, Amirian J, Litovsky S, Smalling R, et al. Intravascular photoacoustic imaging of lipid in atherosclerotic plaques in the presence of luminal blood. Opt Lett. 2012;37:1244–6.
23. Wang P, Wang P, Wang H-W, Cheng J-X. Mapping lipid and collagen by multispectral photoacoustic imaging of chemical bond vibration. J Biomed Opt. 2012;17:096010.
24. Bugs MR, Cornelio ML. Analysis of the ethidium bromide bound to DNA by photoacoustic and FTIR spectroscopy. Photochem Photobiol. 2001;74:512–20.
25. Yao DK, Maslov K, Shung KK, Zhou QF, Wang LV. In vivo label-free photoacoustic microscopy of cell nuclei by excitation of DNA and RNA. Opt Lett. 2010;35:4139–41.
26. Di Primo C, Deprez E, Sligar SG, Hoa GHB. Origin of the photoacoustic signal in cytochrome p-450(cam): Role of the Arg186-Asp251-Lys178 bifurcated salt bridge. Biochemistry. 1997;36:112–8.
27. Zhang C, Zhang YS, Yao DK, Xia Y, Wang LV. Label-free photoacoustic microscopy of cytochromes. J Biomed Opt. 2013;18:20504.
28. Esenaliev RO, Karabutov AA, Oraevsky AA. Sensitivity of laser opto-acoustic imaging in detection of small deeply embedded tumors. IEEE J Sel Top Quantum Electron. 1999;5:981–8.
29. Ku G, Wang LV. Deeply penetrating photoacoustic tomography in biological tissues enhanced with an optical contrast agent. Opt Lett. 2005;30:507–9.
30. Kim C, Erpelding TN, Jankovic L, Pashley MD, Wang LV. Deeply penetrating in vivo photoacoustic imaging using a clinical ultrasound array system. Biomed Opt Express. 2010;1: 278–84.

31. Xing W, Wang L, Maslov K, Wang LV. Integrated optical- and acoustic-resolution photoacoustic microscopy based on an optical fiber bundle. Opt Lett. 2013;38:52–4.
32. Song KH, Wang LV. Deep reflection-mode photoacoustic imaging of biological tissue. J Biomed Opt. 2007;12:060503.
33. Gamelin J, Maurudis A, Aguirre A, Huang F, Guo PY, Wang LV, et al. A real-time photoacoustic tomography system for small animals. Opt Express. 2009;17:10489–98.
34. Xia J, Chatni MR, Maslov K, Guo Z, Wang K, Anastasio M, et al. Whole-body ring-shaped confocal photoacoustic computed tomography of small animals in vivo. J Biomed Opt. 2012;17:050506.
35. Yao J, Kaberniuk AA, Li L, Shcherbakova DM, Zhang R, Wang L, et al. Multiscale photoacoustic tomography using reversibly switchable bacterial phytochrome as a near-infrared photochromic probe. Nat Meth. 2016;13:67–73.
36. Nasiriavanaki M, Xia J, Wan HL, Bauer AQ, Culver JP, Wang LV. High-resolution photoacoustic tomography of resting-state functional connectivity in the mouse brain. Proc Natl Acad Sci U S A. 2014;111:21–6.
37. Yao J, Wang L, Yang JM, Maslov KI, Wong TT, Li L, et al. High-speed label-free functional photoacoustic microscopy of mouse brain in action. Nat Methods. 2015;12:407–10.
38. Fang H, Maslov K, Wang LV. Photoacoustic doppler effect from flowing small light-absorbing particles. Phys Rev Lett. 2007;99:184501.
39. Yao J, Maslov KI, Zhang Y, Xia Y, Wang LV. Label-free oxygen-metabolic photoacoustic microscopy in vivo. J Biomed Opt. 2011;16:076003.
40. Oladipupo S, Hu S, Kovalski J, Yao J, Santeford A, Sohn RE, et al. VEGF is essential for hypoxia-inducible factor-mediated neovascularization but dispensable for endothelial sprouting. Proc Natl Acad Sci U S A. 2011;108:13264–9.
41. Oladipupo SS, Hu S, Santeford AC, Yao J, Kovalski JR, Shohet RV, et al. Conditional HIF-1 induction produces multistage neovascularization with stage-specific sensitivity to VEGFR inhibitors and myeloid cell independence. Blood. 2011;117:4142–53.
42. Agarwal A, Shao X, Rajian JR, Zhang H, Chamberland DL, Kotov NA, et al. Dual-mode imaging with radiolabeled gold nanorods. J Biomed Opt. 2011;16:051307.
43. Chen Y-S, Frey W, Kim S, Homan K, Kruizinga P, Sokolov K, et al. Enhanced thermal stability of silica-coated gold nanorods for photoacoustic imaging and image-guided therapy. Opt Express. 2010;18:8867–78.
44. You J, Zhou J, Zhou M, Liu Y, Robertson JD, Liang D, et al. Pharmacokinetics, clearance, and biosafety of polyethylene glycol-coated hollow gold nanospheres. Part Fibre Toxicol. 2014;11:26.
45. Wang YW, Xie XY, Wang XD, Ku G, Gill KL, O'Neal DP, et al. Photoacoustic tomography of a nanoshell contrast agent in the in vivo rat brain. Nano Lett. 2004;4:1689–92.
46. Li ML, Wang JC, Schwartz JA, Gill-Sharp KL, Stoica G, Wang LV. In-vivo photoacoustic microscopy of nanoshell extravasation from solid tumor vasculature. J Biomed Opt. 2009;14:010507.
47. Yang XM, Skrabalak SE, Li ZY, Xia YN, Wang LHV. Photoacoustic tomography of a rat cerebral cortex in vivo with au nanocages as an optical contrast agent. Nano Lett. 2007;7:3798–802.
48. Song KH, Kim C, Cobley CM, Xia Y, Wang LV. Near-infrared gold nanocages as a new class of tracers for photoacoustic sentinel lymph node mapping on a rat model. Nano Lett. 2009;9:183–8.
49. Agarwal A, Huang SW, O'Donnell M, Day KC, Day M, Kotov N, et al. Targeted gold nanorod contrast agent for prostate cancer detection by photoacoustic imaging. J Appl Phys. 2007;102:064701.
50. Eghtedari M, Liopo AV, Copland JA, Oraevslty AA, Motamedi M. Engineering of heterofunctional gold nanorods for the in vivo molecular targeting of breast cancer cells. Nano Lett. 2009;9:287–91.
51. Eghtedari M, Oraevsky A, Copland JA, Kotov NA, Conjusteau A, Motamedi M. High sensitivity of in vivo detection of gold nanorods using a laser optoacoustic imaging system. Nano Lett. 2007;7:1914–8.

52. Kim K, Huang SW, Ashkenazi S, O'Donnell M, Agarwal A, Kotov NA, et al. Photoacoustic imaging of early inflammatory response using gold nanorods. Appl Phys Lett. 2007;90:223901.
53. Li PC, Wang CRC, Shieh DB, Wei CW, Liao CK, Poe C, et al. In vivo photoacoustic molecular imaging with simultaneous multiple selective targeting using antibody-conjugated gold nanorods. Opt Express. 2008;16:18605–15.
54. Li PC, Wei CW, Liao CK, Chen CD, Pao KC, Wang CRC, et al. Photoacoustic imaging of multiple targets using gold nanorods. IEEE Trans Ultrason Ferroelectr Freq Control. 2007;54:1642–7.
55. Song KH, Kim C, Maslov K, Wang LV. Noninvasive in vivo spectroscopic nanorod-contrast photoacoustic mapping of sentinel lymph nodes. Eur J Radiol. 2009;70:227–31.
56. Melancon MP, Zhou M, Li C. Cancer theranostics with near-infrared light-activatable multimodal nanoparticles. Acc Chem Res. 2011;44:947–56.
57. Lu W, Huang Q, Geng KB, Wen XX, Zhou M, Guzatov D, et al. Photoacoustic imaging of living mouse brain vasculature using hollow gold nanospheres. Biomaterials. 2010;31:2617–26.
58. Lu W, Melancon MP, Xiong C, Huang Q, Elliott A, Song S, et al. Effects of photoacoustic imaging and photothermal ablation therapy mediated by targeted hollow gold nanospheres in an orthotopic mouse xenograft model of glioma. Cancer Res. 2011;71:6116–21.
59. Zhou M, Singhana B, Liu Y, Huang Q, Mitcham T, Wallace MJ, et al. Photoacoustic- and magnetic resonance-guided photothermal therapy and tumor vasculature visualization using theranostic magnetic gold nanoshells. J Biomed Nanotech. 2015;11:1442–50.
60. Sharma P, Brown SC, Bengtsson N, Zhang QZ, Walter GA, Grobmyer SR, et al. Gold-speckled multimodal nanoparticles for noninvasive bioimaging. Chem Mater. 2008;20:6087–94.
61. Ku G, Zhou M, Song SL, Huang Q, Hazle J, Li C. Copper sulfide nanoparticles as a new class of photoacoustic contrast agent for deep tissue imaging at 1064 nm. ACS Nano. 2012;6:7489–96.
62. Zhou M, Song S, Zhao J, Tian M, Li C. Theranostic CuS nanoparticles targeting folate receptors for PET image-guided photothermal therapy. J Mater Chem B. 2015;3:8939–48.
63. Zhou M, Zhang R, Huang M, Lu W, Song S, Melancon MP, et al. A chelator-free multifunctional [^{64}Cu]CuS nanoparticle platform for simultaneous micro-PET/CT imaging and photothermal ablation therapy. J Am Chem Soc. 2010;132:15351–8.
64. Zhou M, Ku G, Pageon L, Li C. Theranostic probe for simultaneous in vivo photoacoustic imaging and confined photothermolysis by pulsed laser at 1064 nm in 4T1 breast cancer model. Nanoscale. 2014;6:15228–35.
65. de la Zerda A, Bodapati S, Teed R, May SY, Tabakman SM, Liu Z, et al. Family of enhanced photoacoustic imaging agents for high-sensitivity and multiplexing studies in living mice. ACS Nano. 2012;6:4694–701.
66. Bouchard L-S, Anwar MS, Liu GL, Hann B, Xie ZH, Gray JW, et al. Picomolar sensitivity MRI and photoacoustic imaging of cobalt nanoparticles. Proc Natl Acad Sci U S A. 2009;106:4085–9.
67. Chamberland DL, Agarwal A, Kotov N, Fowlkes JB, Carson PL, Wang X. Photoacoustic tomography of joints aided by an Etanercept-conjugated gold nanoparticle contrast agent—an ex vivo preliminary rat study. Nanotechnology. 2008;19:095101.
68. Lee HJ, Liu Y, Zhao J, Zhou M, Bouchard RR, Mitcham T, et al. In vitro and in vivo mapping of drug release after laser ablation thermal therapy with doxorubicin-loaded hollow gold nanoshells using fluorescence and photoacoustic imaging. J Controlled Release. 2013;172:152–8.
69. Wang B, Yantsen E, Larson T, Karpiouk AB, Sethuraman S, Su JL, et al. Plasmonic intravascular photoacoustic imaging for detection of macrophages in atherosclerotic plaques. Nano Lett. 2009;9:2212–7.
70. Rouleau L, Berti R, Ng VW, Matteau-Pelletier C, Lam T, Sabourel P, et al. VCAM-1-targeting gold nanoshell probe for photoacoustic imaging of atherosclerotic plaque in mice. Contrast Media Mol Imaging. 2013;8:27–39.
71. Wang B, Joshi P, Sapozhnikova V, Amirian J, Litovsky SH, Smalling R, et al. Intravascular photoacoustic imaging of macrophages using molecularly targeted gold nanoparticles. Proc SPIE 7564. 2010;75640A.

72. Zhou M, Li J, Liang S, Sood AK, Liang D, Li C. CuS nanodots with ultrahigh efficient renal clearance for positron emission tomography imaging and image-guided photothermal therapy. ACS Nano. 2015;9(7):7085–96.
73. Song J, Yang X, Jacobson O, Huang P, Sun X, Lin L, et al. Ultrasmall gold nanorod vesicles with enhanced tumor accumulation and fast excretion from the body for cancer therapy. Adv Mater. 2015;27:4910–7.
74. Yang K, Hu L, Ma X, Ye S, Cheng L, Shi X, et al. Multimodal imaging guided photothermal therapy using functionalized graphene nanosheets anchored with magnetic nanoparticles. Adv Mater. 2012;24:1868–72.
75. Qin H, Zhou T, Yang S, Chen Q, Xing D. Gadolinium(III)-gold nanorods for MRI and photoacoustic imaging dual-modality detection of macrophages in atherosclerotic inflammation. Nanomedicine. 2013;8:1611–24.
76. Lovell JF, Jin CS, Huynh E, Jin H, Kim C, Rubinstein JL, et al. Porphysome nanovesicles generated by porphyrin bilayers for use as multimodal biophotonic contrast agents. Nat Mater. 2011;10:324–32.
77. Kim J-W, Galanzha EI, Shashkov EV, Moon H-M, Zharov VP. Golden carbon nanotubes as multimodal photoacoustic and photothermal high-contrast molecular agents. Nat Nanotechnol. 2009;4:688–94.
78. Zhang YM, Jeon M, Rich LJ, Hong H, Geng JM, Zhang Y, et al. Non-invasive multimodal functional imaging of the intestine with frozen micellar naphthalocyanines. Nat Nanotechnol. 2014;9:631–8.
79. Kircher MF, de la Zerda A, Jokerst JV, Zavaleta CL, Kempen PJ, Mittra E, et al. A brain tumor molecular imaging strategy using a new triple-modality MRI-photoacoustic-Raman nanoparticle. Nat Med. 2012;18:829–34.
80. Guo L, Lei L, Liren Z, Jun X, Wang LV. Multiview Hilbert transformation for full-view photoacoustic computed tomography using a linear array. J Biomed Opt. 2015;20:066010.
81. Zhang HF, Maslov K, Stoica G, Wang LHV. Functional photoacoustic microscopy for high-resolution and noninvasive in vivo imaging. Nat Biotechnol. 2006;24:848–51.
82. Yao J, Maslov KI, Puckett ER, Rowland KJ, Warner BW, Wang LV. Double-illumination photoacoustic microscopy. Opt Lett. 2012;37:659–61.
83. Zhu L, Li L, Gao L, Wang LV. Multiview optical resolution photoacoustic microscopy. Optica. 2014;1:217–22.
84. Zhang C, Maslov K, Yao J, Wang LV. In vivo photoacoustic microscopy with 7.6-μm axial resolution using a commercial 125-MHz ultrasonic transducer. J Biomed Opt. 2012;17:116016.
85. Zhang C, Maslov K, Hu S, Chen R, Zhou Q, Shung KK, et al. Reflection-mode submicron-resolution in vivo photoacoustic microscopy. J Biomed Opt. 2012;17:0205011.
86. Zhang C, Maslov K, Wang LV. Subwavelength-resolution label-free photoacoustic microscopy of optical absorption in vivo. Opt Lett. 2010;35:3195–7.
87. Yao J, Wang L, Li C, Zhang C, Wang LV. Photoimprint photoacoustic microscopy for three-dimensional label-free subdiffraction imaging. Phys Rev Lett. 2014;112:014302.
88. Nedosekin DA, Galanzha EI, Dervishi E, Biris AS, Zharov VP. Super-resolution nonlinear photothermal microscopy. Small. 2014;10:135–42.